PNAS RESEARCH ARTICLE | APPLIED MATHEMATICS

Localized tension–induced giant folding in unstructured elastic sheets

Kexin Guo[a,1], Marc Suñé[b,1], Ming Li Kwok[a], K. Jimmy Hsia[a,c,2], Mingchao Liu[a,d,2], and Dominic Vella[b,2]

Affiliations are included on p. 7.

Edited by John Rogers, Northwestern University, Evanston, IL; received November 14, 2024; accepted April 3, 2025

Buckling in compression is the archetype of elastic instability: when compressed along its longest dimension, a thin structure such as a playing card will buckle out-of-plane accommodating the imposed compression without a significant change of length. However, recent studies have demonstrated that tension applied to sheets with microscopic structure leads to out-of-plane deformation in applications from "groovy metasheets" for multistable morphing to kirigami grippers. Here, we demonstrate that this counterintuitive behavior—a large transverse folding induced by a relatively small imposed longitudinal tension—occurs also in unstructured sheets of isotropic material. The key to this behavior is that a localized uniaxial tension induces giant folding; we refer to this as "localized tension-induced giant (TUG) folding" to reflect the importance of localized tension, and its mode of actuation and the similarity of the loading condition to 'tugging' the sheet. We show that localized TUG folding occurs because of an efficient transfer of applied tensile load into compression—a geometric consequence of a localized applied tension. We determine scaling results for the folding angle as a function of applied strain in agreement with both experiments and simulations. The generic nature of localized TUG folding suggests that it might be utilized in a broader range of materials and structures than previously realized.

buckling | metamaterials | plate theory

Significance

While a slender object is naturally expected to buckle when compressed, other objects (including the bones in human fingers) can achieve the same behavior when pulled. This unusual behavior has been used in applications like soft-robotic grippers, but is often assumed to originate from some unusual microscopic structure e.g. particular patterns of cuts in an otherwise isotropic sheet. We show that the geometry with which the imposed pulling is applied is key, allowing this behavior to be observed even in unstructured, and uniform materials. We use a combination of experiments, mathematical modeling and numerical simulations, to understand its origins and how it can be controlled; this understanding gives insights into the design of such behavior in more complex systems.

Buckling is associated with compressive loads on a slender structure (1); from railway tracks in extreme heat (2) to microtubules in cytoplasm (3), axial compression is relieved by out-of-plane buckling. Given its ubiquity, it is unsurprising that buckling under compression is considered a fundamental mechanism through which structures from bridges to marine and aerospace structures may fail (1, 4). However, other examples have emerged in which an applied tension can lead to a large out-of-plane deformation—the hallmark of buckling. The first examples of this "buckling in tension" to be studied required ingenious design of structures (5), but are now also understood to exist in natural systems such as the luxation of human fingers (6).

At the same time, there has been increased interest in mechanical metamaterials (7, 8): elastic objects with a structure that allows for novel functionality. Several examples of these metamaterials seem to buckle in an orthogonal direction under uniaxial extension; see Fig. 1 *A* and *B*. For example, groovy metasheets (Fig. 1*A*) (9) and kirigami grippers (Fig. 1*B*) (10) look superficially different but both exhibit significant transverse motion upon a small axial extension. Similar behavior can be seen in other systems too, including the ribbed sheet (11), while the leaves of some trees fold as senescence progresses (Fig. 1*C*).

As a first clue that this behavior may not need the careful design that might first be assumed, the reader is invited to crumple a piece of paper, open it out again, clamp the center between thumb and finger and then pull along one axis. As shown in Fig. 1*D*, this informal experiment suggests a similar phenomenology: the paper folds perpendicular to the direction of pulling. A more formal version of this phenomenon has also recently been observed in simulations of (thermal) graphene in which one edge is clamped, leading to extension along this edge (12, 13). This ubiquity of the tensile buckling in these systems (both of which are often modeled as isotropic solids, albeit with modified effective moduli) suggests something more fundamental that has not been reported previously. A clue to the key ingredients may be understood by modifying the crumpled paper example just considered: if instead of pulling at the center with two fingers, the crumpled paper is firmly clamped by hand along its whole width and pulled, no folding is observed.

Perhaps the most striking feature of the examples shown in Fig. 1 *A*–*D* is that a very small and localized tensile deformation in-plane induces a very large folding angle; for this reason we refer to this means of inducing a fold angle as localized Tension–indUced Giant folding, or localized TUG folding, also reflecting the appearance of the phenomenon

Author contributions: K.J.H., M.L., and D.V. designed research; K.G., M.S., M.L.K., M.L., and D.V. performed research; K.G. and M.S. analyzed data; and K.G., M.S., M.L., and D.V. wrote the paper.

The authors declare no competing interest.

This article is a PNAS Direct Submission.

[1]K.G. and M.S. contributed equally to this work.

[2]To whom correspondence may be addressed. Email: kjhsia@ntu.edu.sg, m.liu.2@bham.ac.uk, or dominic.vella@maths.ox.ac.uk.

This article contains supporting information online at https://www.pnas.org/lookup/suppl/doi:10.1073/pnas.2423439122/-/DCSupplemental.

Published May 12, 2025.

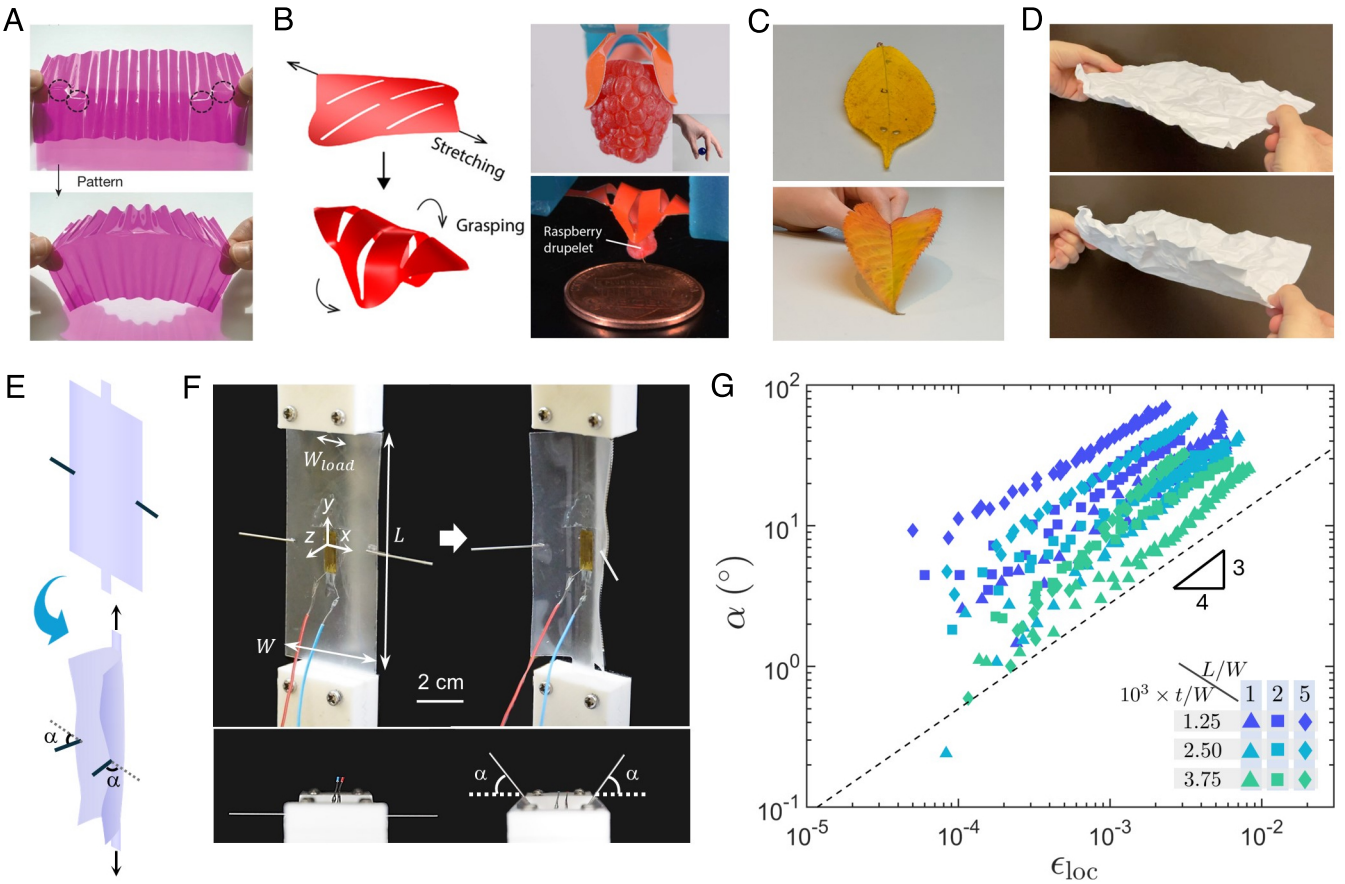

Fig. 1. Uniaxial, localized tension leads to transverse buckling in a range of structured and unstructured thin sheets. (*A*) A groovy plastic sheet is stretched by a point force along the horizontal direction and forms a scar along which the sheet bends and fods. Adapted from ref. 9 with permission from Springer Nature. (*B*) A soft gripper made of a kirigami shell is actuated by stretching along the midline to grasp a raspberry. Adapted from ref. 10 (Reprinted with permission from AAAS). (*C*) Leaves of the flowering cherry (*Prunus "kanzan"*) show a similar folding at different stages of leaf senescence from early (*Top*) to mid (*Bottom*). (*D*) A crumpled paper sheet is stretched along the horizontal direction by a localized force, and demonstrates folding in the transverse direction. (*E*) Schematic of the experimental setup. A rectangular planar sheet is clamped at the additional "tabs" centered on each short side (*Upper* diagram). The sheet folds transversally, developing a nonzero fold angle α, as the clamps are displaced to impose a longitudinal displacement (*Lower* diagram). (*F*) Our experimental setup and associated geometrical parameters of the sheet. Side (*Upper* snapshots) and zenithal view (*Lower* snapshots) of the planar, unloaded, sheet (*Left*), and the loaded sheet when it folds in the transverse direction (*Right*). (*G*) Experimentally measured inclination angles α as a function of the local tensile strain, ϵ_{loc}, measured by a strain gauge for a PVC sheet. Plotting on a doubly logarithmic scale for sheets of various dimensions reveals the power-law relationship $\alpha \propto \epsilon_{loc}^{3/4}$, which we seek to explain in this article. For all specimens shown here, $W = 40$ mm, $W_{load}/W = 1/4$, and other geometric parameters are listed in the legend. The Young's modulus is approximately 3 GPa from tensile test measurements on fully clamped strips (*SI Appendix*, Fig. S1*C*); the Poisson's ratio $\nu \approx 0.38$ for PVC materials.

when "tugging" an elastic sheet. In this paper, we use a combination of experiments, numerical simulations and mathematical modeling to understand the origin of localized TUG folding.

Through the application of the Föppl-von Kármán (FvK) plate theory (14), we examine both the onset of out-of-plane deformation (the near-threshold regime) and its evolution far beyond the critical imposed strain [the far-from-threshold regime (15–17)]. We derive the scaling law for the inclination angle as a function of the applied strain that explains the results in experiments and simulations. This scaling law provides useful insight into the geometry and material properties that allow for a large actuation of an elastic sheet.

Importance of Localized Tension

The difference between pulling at a point vs. along the full edge motivates only using a localized pulling force. Indeed, similar phenomenology can be observed by taking a uniform sheet and stretching with a small clamped region at the center (Fig. 1*E*). [In the case of uniform clamping along the whole edge, the sheet remains planar—see the numerical simulations of a stretched sheet with fully clamped edges in *SI Appendix*, Fig. S3*B*—suggesting that this behavior occurs at much smaller strains than are required to cause global wrinkling (15, 16).] This phenomenology cannot, therefore, be caused only by the structure, cuts or folds, in the examples already discussed (Fig. 1 *A*–*D*). We therefore focus on experimental realizations in which a small region along the axis is loaded in sheets that are unstructured (i.e. spatially homogeneous and isotropic).

In our experiments, we use rectangular sheets of polyvinyl chloride (PVC), with uniform thickness t, that are laser cut with length L and width W and an additional "tab" (of width $W_{load} =$ 10 mm and length $L_{load} = 30$ mm) on each side to ensure that a localized uniform clamping can be applied. The dimensions of the rectangular sheet (excluding the tab) are varied ensuring that the resulting sheet has $L/W \geq 1$ with $W/t \gg 1$; see Fig. 1*F*. (Further details of the sheets used in experiments may be found in *Materials and Methods* and *SI Appendix*; further images of our experimental setup are shown in *SI Appendix*, Fig. S1.) The rectangular sheets are clamped by the tabs in 3D-printed fixtures that are attached onto mechanical sliders (Fig. 1*F*). The supports are displaced along the y-axis by a distance

$$\Delta u_y \equiv u_y(x=0, y=L/2) - u_y(x=0, y=-L/2) > 0. \quad [1]$$

If the sheet remained planar, so that its mid-plane $z = 0$ (Fig. 1*F*), this imposed displacement would lead to a planar strain

$$\epsilon_0 = \frac{\Delta u_y}{L}. \quad [2]$$

However, once the strain reaches a small threshold value, the sheet curls in both x and y directions so that the mid-plane of the sheet is deformed to $z = \zeta(x, y)$. Double curving is displayed by a projected laser line along the two midlines at $x = 0$ and at $y = 0$—images are included in *SI Appendix*, Fig. S1 *E* and *F*—and distinguishes this effect from the edge clamping-induced tilting of graphene (12, 13), in which the imposed boundary condition inhibits this double curving. Fig. 1 *E* and *F* show the transverse curving as viewed with small cannula needles attached to the edge of the sheet; these needles allow us to measure the angle, α, that the edge of the sheet makes with the horizontal.

Scaling Behavior of Folding

The angle, α, that the edge of the sheet makes with the horizontal is measured as a function of imposed strain; see Fig. 1*G*. (Here the value of the strain is measured using a strain gauge placed at the center of the sample, which gives a measure of the local strain ϵ_{loc}—see *Materials and Methods*.) The experimental results of Fig. 1*G* suggest that $\alpha \propto \epsilon_{\text{loc}}^{3/4}$—a scaling that is also consistent with similar experiments on crumpled paper (*SI Appendix*, Fig. S2). Two features of this scaling are particularly noteworthy. First, we reiterate that $\epsilon_{\text{loc}} > 0$—the sheet is subject to a tensile load and yet buckles in the transverse direction. Second, this scaling is more sensitive to the imposed end-stretching than the regular (compressive) buckling in which, for example, the amplitude $A \propto \Delta u_y^{1/2}$ (18) where Δu_y is the imposed end-shortening defined in Eq. **1**.

To test whether this behavior is indeed generic, or is caused by some imperfection or anisotropy of the experimental system, we also performed systematic numerical simulations using the finite element method (FEM) software ABAQUS. The results of our FEM simulations allow the deformed shape $\zeta(x, y)$ to be calculated. In particular, the observed inclination angle is plotted as a function of the mean strain

$$\bar{\epsilon} = \epsilon_0 + \frac{1}{2L}\int_{-L/2}^{L/2}\left(\frac{\partial \zeta}{\partial y}\right)^2 \mathrm{d}y, \quad [3]$$

in Fig. 2*B*. These results demonstrate that the key phenomenology is similar: out-of-plane bending occurs transverse to the imposed stretching (see Fig. 2*A*, which displays $\zeta(x, 0)$, the vertical displacement along the midline at $y = 0$), while the angle of inclination, α, follows a power-law similar to that observed experimentally, cf. Fig. 1*G*. Numerical simulations allow us to test the role of the Poisson's ratio ν; our results show a small effect of ν but, crucially, that the effect persists as $\nu \to 0$ (Fig. 2*B*). This is in contrast with the tensional wrinkling experiment of Cerda and Mahadevan (CM) (16) for which the effect disappears entirely as $\nu \to 0$ (19, 20). We further discuss the role of the Poisson effect in the subsequent theoretical analysis.

One important difference between experiments and these numerical simulations is that we observe a small (experimentally undetectable), and $\bar{\epsilon}$-independent, angle for very small stretching with a sharp transition to a larger, $\bar{\epsilon}$-dependent, α, at some critical strain, $\bar{\epsilon}_c$. Note that this transition is not observable in experiments because of the limited angular resolution, which is caused by small fluctuations in the initial state. We therefore seek to understand both the emergence of a critical strain, $\bar{\epsilon}_c$, and the scaling of the angle α when $\bar{\epsilon} > \bar{\epsilon}_c$.

Our experiments and numerical simulations show a wide range of inclination angles $0.01° \lesssim \alpha \lesssim 100°$ at small imposed strains—the axial strain is at most $\bar{\epsilon} \sim 10^{-2}$ in Figs. 1 and 2. The conjunction of large out-of-plane deflections and small strains is a common feature of thin sheets and is encapsulated in the FvK plate theory, which combines a mechanically linear response (i.e. a Hookean stress–strain relationship) with nonlinear displacement–strain relationships (i.e. out-of-plane

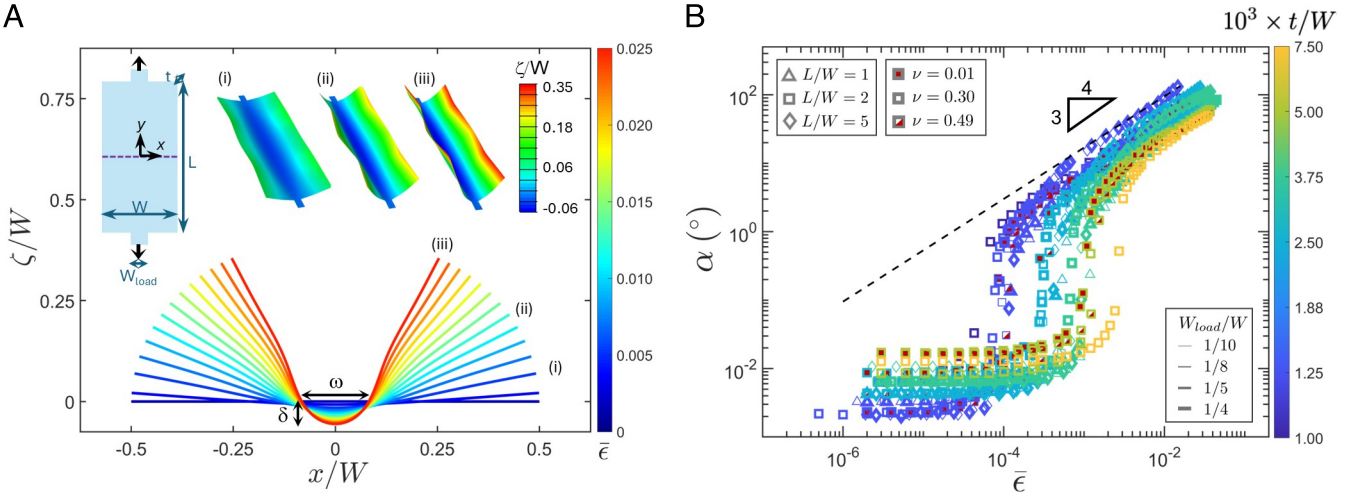

Fig. 2. Finite element simulations of tensile stretching induced folding in elastic sheets. (*A*) Cross-sectional profiles, $\zeta(x, 0)$, of a sheet stretched along the y-axis in normalized units. The color bar indicates the tensile strain of the midline at $x = 0$ (see *Top-Left Inset*). The *Top-Right Insets* (i–iii) show the deformed shapes of the elastic sheet at increasing strains, with corresponding numbers labeled in the cross-sectional profiles, and colors indicating the ζ-displacements normalized by W according to the color bar. The model shown here has the following geometric and material parameters: $L/W = 2$, $t/W = 2.5 \times 10^{-3}$, $W_{\text{load}}/W = 1/10$, $E = 3$ GPa, and $\nu = 0.3$. (*B*) Simulation results of tensile strains and inclination angles for elastic sheets with various geometric parameters and Poisson's ratio, as indicated in the legend. The color bar indicates the thickness-to-width (t/W) ratio. These numerical results suggest that $\alpha \propto \bar{\epsilon}^{3/4}$ (dashed line), as also observed experimentally. Note that in (*B*) the marker style is used to encode the geometry and Poisson's ratio used in simulations (as indicated by the grayscale legends). Color is used to encode the thickness (as per the colorbar on the *Right* hand side).

displacements contribute to strains) (14). The coupling of the stress field within the sheet to the sheet's shape in the FvK equations makes analytical progress difficult. A key simplification comes while the sheet remains planar: we then need only solve for the stress within the loaded sheet and the characteristic tension is linear in the imposed end separation,

$$T_0 = Y\epsilon_0, \qquad [4]$$

where $Y = E\,t$ is the stretching modulus; E denotes the Young's modulus, which is measured experimentally (*SI Appendix*), but does not directly control this geometrical effect. The problem for the planar stress can be posed as the biharmonic equation for the Airy stress function χ with appropriate boundary conditions (*SI Appendix*, *Mathematical Model*). The resulting equations can be analyzed using Laplace transform methods (21–23) (see *SI Appendix* for details). The key result of this analysis is that, for sufficiently slender sheets at least, and for $W_{\text{load}} \ll W$, the stress components within the sheet remain tensile except within a small region close to the edges (i.e. within a typical distance W from the short edges the transverse stress is compressive) (*SI Appendix*, Fig. S9). Moreover, this analysis allows us to compare the effect of point-loading, $W_{\text{load}} \ll W$, with the more common full-width loading, $W_{\text{load}} = W$, in the limit of vanishing Poisson ratio $\nu \to 0$. This comparison (*SI Appendix*, Fig. S12) shows that the zone of compression persists with point-loading but disappears with full-width loading—the geometry of the loading is key to the localized TUG-folding demonstrated here and distinguishes it from the tensional wrinkling studied extensively previously (16). In addition, this effect does not require a negative Poisson ratio, as might be inferred on the basis of the tilt phase in clamped thermal graphene (12). The origin of this compression signals the importance of a "mechanism" in generating the compression (*SI Appendix*, Fig. S12).

The linearity of this planar problem for the stress prior to buckling, means that the magnitude of the compressive stress generated by "tugging" must be linear in the characteristic tension T_0. The coincidence of lengths (i.e. that the lateral scale of the compressed area scales with W) and of stresses (i.e. that the resulting transverse compression is linear in the characteristic tension, T_0) simplifies the near-threshold analysis of instability (19) so that the classic Euler-like buckling analysis is helpful (see *SI Appendix*, *Mathematical Model* for details). Hence, we expect that buckling will occur when T_0 reaches some multiple of B/W^2, which immediately gives us that

$$\epsilon_0^c = \bar{\epsilon}_c \propto \frac{B}{YW^2}. \qquad [5]$$

For the unstructured, isotropic sheets used here, the bending modulus $B = Yt^2/[12(1-\nu^2)]$ and so Eq. **5** predicts that

$$\epsilon_0^c = \bar{\epsilon}_c \propto \frac{t^2}{(1-\nu^2)W^2}, \qquad [6]$$

which may be interpreted as the reciprocal of the von Kármán number (24). We emphasize that the scalings for the critical strain in Eqs. **5** and **6** are the standard scalings for Euler buckling (12, 25)—we shall see later that they are borne out by detailed numerical simulations, which serve to show that this transition is indeed driven by buckling.

We also observe that the sheet is doubly curved in a narrow region (Fig. 2*A*); outside this doubly-curved region, there is a small curvature in the y-direction (along the pulling direction), while in the x-direction, the sheet is essentially flat (albeit inclined at the angle α)—in this sense the response of the sheet to uniaxial tension is to fold in the transverse direction. We denote the (unknown) width of this doubly-curved region by ω (Fig. 2*A*) and estimate it using the experimental (and numerical) observation of the shape to pose an ansatz for the sheet's out-of-plane displacement, $\zeta(x,y)$, relative to the initially planar state; in particular, we take:

$$\zeta(x,y) = \delta \times \begin{cases} \cos\frac{\pi y}{L}\cos\frac{\pi x}{\omega}, & |x| < \omega/2, \\ \frac{\pi}{\omega}\left(\frac{\omega}{2} - |x|\right), & \omega/2 \le |x| \le W/2, \end{cases} \qquad [7]$$

where δ is the maximum amplitude (Fig. 2*A*), and the constants have been chosen to ensure that the vertical displacement, slope, and curvature of the sheet are all continuous at the edge of the curved central region. (Note that this ansatz is only appropriate for $W_{\text{load}} \ll \omega$, since otherwise a third region would be required.) To determine ω, we note that the smaller its value, the more curved the sheet is in the central region, and the higher its bending energy is $U_{\text{bend}} \sim B\int(\nabla^2\zeta)^2 \mathrm{d}A \sim B\delta^2 L/\omega^3$ (where we have neglected the bending energy caused by the curvature in the y-direction because $L \gtrsim W \gg \omega$). Conversely, the excess stretching energy caused by being doubly curved is localized to this central region so that $U_{\text{stretch}} \sim \int \sigma : \epsilon \,\mathrm{d}A \sim WL\bar{T}^2/Y + \omega L\bar{T}\delta^2/L^2$, where the characteristic tension, $\bar{T}$, is linear in the mean strain,

$$\bar{T} = Y\bar{\epsilon}, \qquad [8]$$

and we make the common assumption that the sheet buckles in the compressing (x) direction to relax the compressive stress. Notice also that there are two different length scales for the two terms in U_{stretch}: the whole sheet, of width W, feels the longitudinal tension, but only the narrow strip, of width ω, is subject to the additional strain, $\sim \delta^2/L^2$, from double-curvature. In the first term in U_{stretch}, we also assume that $\epsilon_0 \sim \bar{\epsilon} = \bar{T}/Y$ remains true after buckling, by virtue of the observation that $\bar{\epsilon} - \epsilon_0 \propto \epsilon_0 - \bar{\epsilon}_c$ sufficiently close to the buckling threshold ($(\bar{\epsilon} - \bar{\epsilon}_c)/\bar{\epsilon}_c \lesssim 10$—see the numerical simulation results for the mean strain beyond buckling in *SI Appendix*, Fig. S6*B*). The total elastic energy, $U_{\text{bend}} + U_{\text{stretch}}$, is then minimized when

$$\omega \propto \left(\frac{BL^2}{\bar{T}}\right)^{1/4} = \left(\frac{BL^2}{Y\bar{\epsilon}}\right)^{1/4}. \qquad [9]$$

Note that the scaling law for the width of the curved region, Eq. **9**, is identical to the scaling for the wavelength of wrinkling observed when a sheet has its whole width clamped and is then pulled perpendicular to this width, as studied by CM (16). We will discuss the similarities and the differences between our results and CM later in the text.

Geometry gives that the inclination angle satisfies $\alpha \approx \tan\alpha = \pi\delta/\omega$ in which ω has been determined (at least to a scaling level) by the previous argument and we assume $\alpha \ll 1$ for consistency with our use of the FvK formalism; the final part of the puzzle therefore is to determine the maximum amplitude δ in Eq. 7. We note that our numerics show that, even after onset, $\bar{\epsilon} \propto \epsilon_0$ (*SI Appendix*, Fig. S6*B*). As a result, we have that $\delta^2/L^2 \propto \bar{\epsilon} - \bar{\epsilon}_c$ and $\delta \propto L(\bar{\epsilon} - \bar{\epsilon}_c)^{1/2}$, which, when combined with the geometrical relationship $\alpha \approx \pi\delta/\omega$, gives us that

$$\alpha \propto \delta\left(\frac{Y\bar{\epsilon}}{BL^2}\right)^{1/4} \propto \left(\frac{YL^2}{B}\right)^{1/4}\bar{\epsilon}^{1/4}(\bar{\epsilon} - \bar{\epsilon}_c)^{1/2}. \qquad [10]$$

Using Eq. **6**, this result may also be written

$$\alpha \propto \frac{tL^{1/2}}{W^{3/2}\sqrt{1-\nu^2}} \left(\frac{\bar{\epsilon}}{\bar{\epsilon}_c}\right)^{1/4} \left(\frac{\bar{\epsilon}}{\bar{\epsilon}_c} - 1\right)^{1/2}. \qquad [11]$$

Here, we have employed an empirical observation, based on our numerics, to understand the scaling of the amplitude δ with strain. Beyond threshold, the nonlinear coupling between strain and vertical displacement hinders analytical progress such that even approximate theories based on the FvK framework, e.g. tension field theory [see e.g. the work of Xin and Davidovitch (20) on the CM problem (16)], ultimately require numerical resolution.

To highlight the trend that $\alpha \to 0$ as $\bar{\epsilon} \searrow \bar{\epsilon}_c$, we rescale the x-axis in Fig. 3 on the basis of the predicted scaling for $\bar{\epsilon}_c$ given in Eq. **6**; Eq. **10**, in turn, suggests a rescaling for the inclination angle on the y-axis. The results plotted in this way show a reasonable collapse (Fig. 3). The experimental data points in this figure are plotted using an effective mean strain obtained by the linear relation in *SI Appendix*, Fig. S5*A* to keep a consistent strain definition with the numerics; a similar collapse is observed when plotting ϵ_{loc} in the experimental results (see the collapse of the inclination angle in *SI Appendix*, Fig. S5*B*).

Critical Strain for Buckling. The prediction for the inclination angle also gives us a more precise means to determine the threshold strain for buckling in our FEM simulations: except very close to the buckling transition, we expect $\alpha \propto (\bar{\epsilon} - \bar{\epsilon}_c)^{3/4}$ and so plot $\alpha^{4/3}$ as a function of $\bar{\epsilon}$ (Fig. 4*A*). This plot shows the expected linear behavior and also allows us to determine the threshold strain, $\bar{\epsilon}_c$, as a function of the sheet thickness ratio, t/W, and Poisson's ratio ν. The resulting plot (Fig. 4*B*) shows that the prediction of Eq. **6** is borne out in our numerical simulations, although points with $L = W$ do not collapse as well as those points with $L/W \gg 1$. We also note that extrapolating this critical strain to the experimentally relevant values of t/W suggests the typical onset strain in experiments is around 10^{-4}, which for a sample with $L = 10$ cm, corresponds to a displacement $\Delta u_y \approx 10$ μm. This, in addition to the very small angles close to onset already noted, explains why this threshold behavior is not visible in our experiments.

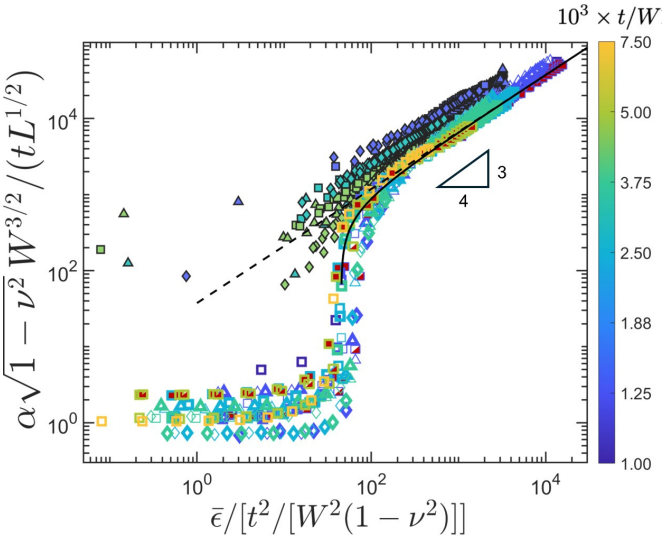

Fig. 3. Master curve for inclination angle, α (°), as a function of mean strain, $\bar{\epsilon}$. Here, results are shown for both simulations and experiments with rescalings suggested by the critical strain at buckling, Eq. **6**, and the scaling for inclination angle Eq. **11**. The dashed line shows the expected scaling behavior for $\bar{\epsilon} \gg \bar{\epsilon}_c$ while the solid curve shows the result Eq. **11** assuming a prefactor of 43 in Eq. **6**. (The same legends as in Fig. 2*B* are adopted for simulation data, i.e. marker shapes denote the aspect ratio, marker fill indicates the Poisson's ratio, marker line-widths denote W_{load}/W and color indicates the sheet thickness as per the color bar.) Experimental data points are shown behind the simulation data in black-bordered markers with fill colors corresponding to the sheet thickness and shapes denoting the aspect ratio. (The experimentally measured strain ϵ_{loc} has been converted to an effective mean strain $\bar{\epsilon}_{\text{eff}}$ based on simulation results—see the plot of ϵ_{loc} vs. $\bar{\epsilon}$ in *SI Appendix*, Fig. S5. Moreover, to avoid cluttering the plot, prior to buckling every second data point from each simulation is displayed while in the postbuckling regime every eighth data point is displayed).

Comparing the critical buckling behavior in our problem (Fig. 4*B*) and in models of the CM problem (e.g. figure 7A of ref. 19), we note that both have identical scaling behavior with thickness and width of the sheet. However, the effect described here persists even with no Poisson effect vanishes, i.e. in the limit of vanishing Poisson ratio $\nu \to 0$, in contrast to the CM problem. Moreover, we find that the threshold value of the dimensionless control parameter $\bar{\epsilon}_c$ is smaller than that in the CM problem (19); for example, comparing the critical strains with $\nu = 0.32$ and $t/W = 10^{-4}$ we have

$$\frac{T_0^c}{Y} \approx \frac{t^2}{W^2} \times \begin{cases} 43/(1-\nu^2), & W_{\text{load}} \ll W, \\ 9 \times 10^4 & W_{\text{load}} = W. \end{cases} \qquad [12]$$

(Here, the critical value for the full-width case, $W_{\text{load}} = W$, comes from figure 7A of ref. 19, while the critical value for $W_{\text{load}} \ll W$ comes from our numerical results in Fig. 4*B*.) Note that with the load applied across the full width, the threshold strain required to trigger buckling is more than 1,000 times larger than in the localized case considered here. To understand this apparently enhanced resistance to buckling in the CM problem, we compare the maximum compressive stress in the full-width setup (as calculated in ref. 19) with that in our problem (see the details of *SI Appendix*, *Mathematical Model*). For the specific case of $L/W = 4$ and $\nu = 0.3$, we find (*SI Appendix*, Fig. S12) that

$$\max_y \left\{\frac{-\sigma_{xx}}{T_0}\right\} \approx \begin{cases} 0.6, & W_{\text{load}} \ll W, \\ 0.006, & W_{\text{load}} = W. \end{cases} \qquad [13]$$

The magnitude of the maximum compressive stress is hence 100 times larger in the localized loading case considered here than in the full-width case. Recalling that the critical strain was 1,000 times larger for the full-width case, we deduce that much of the difference in critical imposed strain can be attributed to the increased efficiency of focusing the longitudinal tensile strain into a transverse compression when pulling with a localized load than over the full-width. However, there also remains an effect of the boundary conditions on the relevant Euler buckling load—indeed, even a standard buckling analysis gives an increase of a factor of 4 between the critical load for a simply supported beam (analogous to the freer edges here) and a clamped beam (analogous to the more constrained edges of the CM problem) (14).

We also found that the scaling for the width of the curved region in Eq. **9** is equivalent to the wavelength of wrinkles in CM (16). While we emphasize that, for the narrow loading $W_{\text{load}} \ll \omega$ we studied here, only a single depression is formed (equivalent to half a wavelength), this equivalence suggests that the narrow curved strip is effectively wrinkling around the narrowly loaded part. If we relax the assumption $W_{\text{load}}/\omega \ll 1$—by imposing longitudinal strains large enough that $\omega \sim W_{\text{load}}$, for example—we observe wrinkles in the curved part of the sheet (*SI Appendix*, Fig. S13). However, we emphasize that the localy-loaded sheet and the fully clamped sheet have significant

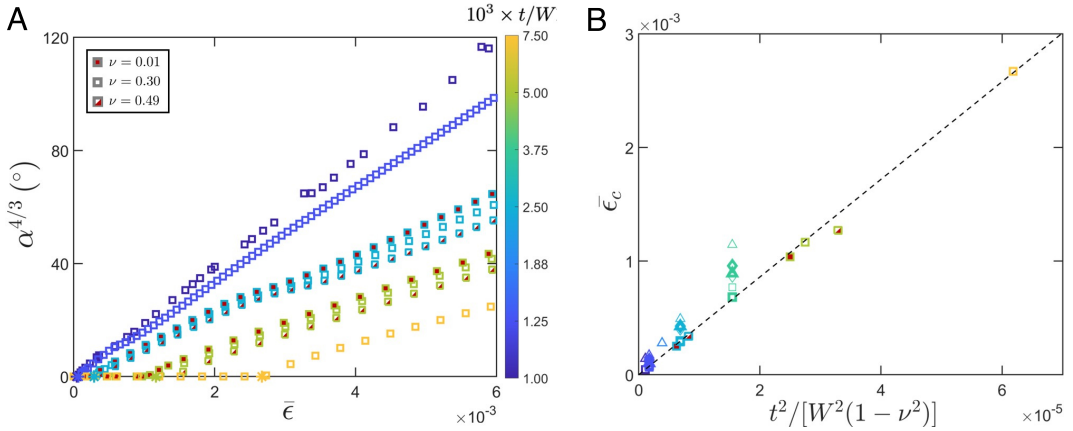

Fig. 4. Critical buckling behavior in FEM simulations. (*A*) The inclination angle α allows for a clearer determination of the critical strain for buckling in our FEM simulations. Buckling occurs where the linear region of the scaled inclination angle intersects with the *x*-axis, which defines the critical buckling strain $\bar{\epsilon}_c$. The curves shown all have $L/W = 2$, $W_{load}/W = 1/5$, with various sheet thickness ratios as indicated by the color bar. (*B*) The critical strains for various geometric parameters and Poisson's ratios ν are proportional to the ratio $B/(YW^2) \propto (t/W)^2/(1-\nu^2)$; the dashed line shows the relationship Eq. **6** with coefficient of proportionality 43.

differences in that localized TUG folding persists as $\nu \to 0$ and the sheet must be loaded to large strains to observe full-width wrinkling.

Conclusions

We have shown that localized tensile loading of an unstructured elastic sheet along one axis actuates folding in an orthogonal direction by inducing compression. A particularly striking feature of this transformation from tension to compression is that it allows a very small and localized strain to actuate a giant folding angle: what we call "localized TUG folding." We claim that a similar mechanism has been observed, if not directly reported, in structured materials—such as a crumpled sheet of paper (Fig. 1*D*), kirigami shells (10), and groovy plastic sheets (9)—but to our knowledge has not been reported in homogeneous, isotropic materials. While our scaling laws for the critical strain and inclination angle reveal how the geometry of the sheet and the properties of the material should be tuned to actuate a homogeneous sheet, in the same way, they also give insights into the mechanisms by which the various metasheets (in the examples mentioned above) are able to achieve localized TUG folding. We note that these all involve structures (albeit different in nature) that make stretching in one direction easier but making bending in the transverse direction more difficult. For example, the ridges of a crumpled piece of paper buffer excess length (26) (reducing the effective Y), while also increasing the effective thickness [and hence increasing the effective B (27)], and similarly for the perpendicular cuts and grooves in kirigami grippers and groovy metasheets, respectively. In an unstructured sheet, the combination of a decreased stretching modulus and an increased bending modulus results in an increased buckling strain—see Eq. **5**. However, at a given multiple of the strain threshold, $\tilde{\epsilon} = \bar{\epsilon}/\bar{\epsilon}_c$, this increase in $B/(YW^2)$ becomes helpful in achieving localized TUG folding; in particular, we note that Eq. **10** may be rewritten:

$$\alpha \propto \left(\frac{B}{YW^2}\right)^{1/2} \left(\frac{L}{W}\right)^{1/2} \tilde{\epsilon}^{1/4}(\tilde{\epsilon}-1)^{1/2}, \qquad [14]$$

and so, for a given $\tilde{\epsilon}$, large $B/(YW^2)$, combined with $L/W \gg 1$, leads to a large folding angle.* A second key ingredient therefore is the geometrical focusing that reduces the critical $\bar{\epsilon}_c$ by a factor of $\sim 10^3$ compared to the fully clamped case (Eq. **12**). The efficiency of this conversion from tension to transverse compression means that a given strain leads to a large α; in addition, if Y is decreased by structure, such as cuts, or by the microscopic "buffering" of area (26), such as crumples or excess area (12, 13), then a fixed load will lead to a still larger strain and hence even larger folding angle. This fundamental insight opens the door for designing structures that can more readily demonstrate localized TUG folding with, or without, structure. It may also lead to new insights into similar phenomenology in systems as diverse as dimpled sheets [which fold upon "snapping" of the dimples along a line (28)] to tension-induced buckling in active systems (29).

*Note that Eq. **14** is similar to the result Eq. **11** except that for more general, possibly structured, solids, we do not assume that $B \propto Yt^2$.

Materials and Methods

Sample Preparation. Test specimens were prepared from commercial PVC films with thickness $t \in \{40, 100, 150\}$ μm. Rectangular sheets were laser cut with width $W = 40$ mm, length $L \in \{40, 80, 200\}$ mm, and two tabs with width $W_{load} = 10$ mm and length $L_{load} = 30$ mm at each end (*SI Appendix*, Fig. S1*B*). The fixtures were then attached to the blocks of two linear-stage motors that were controlled manually. The specimens were clamped at the tabs in 3D-printed clamp fixtures designed with teeth on the inner surfaces to reduce slipping. Prior to clamping the specimen, strain gauges with a gauge length of 6 mm, resistance of 350 Ω, and resolution of 1 με (Tokyo Measuring Instruments Laboratory, GFLA-6-350-70) were adhered to the center of the specimen using strain gauge adhesives (Tokyo Measuring Instruments Laboratory). The measured strain data were recorded by a data logger (Tokyo Measuring Instruments Laboratory, TDS-303). Inclination angles of the sheets were measured from photographs taken from the orthogonal plane (see *SI Appendix, Experimental Methods* for further details) with the assistance of cannula needles adhered to the edges of the sheet. The needle lines were detected using MATLAB scripts; the inclination angles reported are the mean values of the left and right sides.

Numerical Simulations. Numerical simulations were conducted using the commercial finite element analysis software ABAQUS/2023. The solid was represented by S4R shell elements and a linear elastic constitutive relation was applied with Young's modulus $E = 3{,}000$ MPa; most simulations were performed with Poisson's ratio $\nu = 0.3$, though results with $\nu = 0.01$ and $\nu = 0.49$ are also reported. The boundary conditions were set as in the experiment: the top edge of the upper tab was fully fixed, while displacement loading was applied along the *y*-axis to the bottom edge of the lower tab. Two analysis steps were conducted in sequence: first, a small out-of-plane displacement were applied to the midline along $x = 0$ with a magnitude of

∼1% of sheet thickness, introducing initial imperfections to the sheet; second, the static analysis step was performed for the process of tensile stretching and sheet folding.

Data, Materials, and Software Availability. All study data are included in the article and/or *SI Appendix*.

ACKNOWLEDGMENTS. This work was partially supported by the UK Engineering and Physical Sciences Research Council via Grant No. EP/Y027949/1 (M.S. and D.V.); the Ministry of Education (MOE), Singapore, via MOE Academic Research Fund Tier 3 Award MOE-MOET32022-0002 (K.G. and K.J.H.); the Presidential Postdoctoral Fellowship from Nanyang Technological University, Singapore, and the start-up funding from the University of Birmingham, UK (M.L.). We thank Ms. Mariona Caus for assisting in taking the pictures in Fig. 1*D*.

Author affiliations: [a]School of Mechanical and Aerospace Engineering, Nanyang Technological University, Singapore 639798, Singapore; [b]Mathematical Institute, University of Oxford, Oxford OX2 6GG, United Kingdom; [c]School of Chemistry, Chemical Engineering and Biotechnology, Nanyang Technological University, Singapore 639798, Singapore; and [d]Department of Mechanical Engineering, University of Birmingham, Birmingham B15 2TT, United Kingdom

1. P. M. Reis, A perspective on the revival of structural (in) stability with novel opportunities for function: From Buckliphobia to Buckliphilia. *J. Appl. Mech.* **82**, 111001 (2015).
2. G. P. Pucillo, Thermal buckling and post-buckling behaviour of continuous welded rail track. *Int. J. Vehic. Sys. Dyn.* **54**, 1785–1807 (2016).
3. C. P. Brangwynne *et al*., Microtubules can bear enhanced compressive loads in living cells because of lateral reinforcement. *J. Cell Bio.* **173**, 733–741 (2006).
4. R. M. Jones, *Buckling of Bars, Plates, and Shells* (Bull Ridge Corporation, 2006).
5. D. Zaccaria, D. Bigoni, G. Noselli, D. Misseroni, Structures buckling under tensile dead load. *Proc. R. Soc. A* **467**, 1686–1700 (2011).
6. M. Fraldi, S. Palumbo, A. Cutolo, A. R. Carotenuto, D. Bigoni, Bimodal buckling governs human fingers' luxation. *Proc. Natl Acad. Sci. USA* **120**, e2311637120 (2023).
7. K. Bertoldi, V. Vitelli, J. Christensen, M. Van Hecke, Flexible mechanical metamaterials. *Nat. Rev. Mater.* **2**, 1–11 (2017).
8. P. Jiao, J. Mueller, J. R. Raney, X. Zheng, A. H. Alavi, Mechanical metamaterials and beyond. *Nat. Commun.* **14**, 6004 (2023).
9. A. Meeussen, M. van Hecke, Multistable sheets with rewritable patterns for switchable shape-morphing. *Nature* **621**, 516–520 (2023).
10. Y. Yang, K. Vella, D. P. Holmes, Grasping with kirigami shells. *Sci. Robot.* **6**, eabd6426 (2021).
11. E. Siéfert, N. Cattaud, E. Reyssat, B. Roman, J. Bico, Stretch-induced bending of soft ribbed strips. *Phys. Rev. Lett.* **127**, 168002 (2021).
12. Z. Chen, D. Wan, M. J. Bowick, Spontaneous tilt of single-clamped thermal elastic sheets. *Phys. Rev. Lett.* **128**, 028006 (2022).
13. R. A. Valenzuela, P. Hanakata, M. J. Bowick, Geometric control of tilt transition dynamics in single-clamped thermalized elastic sheets. *Phys. Rev. E* **128**, 028006 (2023).
14. L. D. Landau, E. M. Lifshitz, *Theory of Tlasticity* (Elsevier, 1986).
15. E. Cerda, K. Ravi-Chandar, L. Mahadevan, Thin films: Wrinkling of an elastic sheet under tension. *Nature* **419**, 579–580 (2002).
16. E. Cerda, L. Mahadevan, Geometry and physics of wrinkling. *Phys. Rev. Lett.* **90**, 074302 (2003).
17. B. Davidovitch, R. D. Schroll, D. Vella, M. Adda-Bedia, E. A. Cerda, Prototypical model for tensional wrinkling in thin sheets. *Proc. Natl. Acad. Sci. U.S.A.* **108**, 18227–18232 (2011).
18. P. Howell, G. Kozyreff, J. Ockendon, *Applied Solid Mechanics* (Cambridge University Press, Cambridge, UK, 2008).
19. M. Xin, B. Davidovitch, Stretching Hookean ribbons part I: Relative edge extension underlies transverse compression and buckling instability. *Euro. Phys. J. E* **44**, 92 (2021).
20. M. Xin, B. Davidovitch, Stretching Hookean ribbons part II: From buckling instability to far-from-threshold wrinkle pattern. *Euro. Phys. J. E* **44**, 94 (2021).
21. M. L. Williams, Stress singularities resulting from various boundary conditions in angular corners of plates in extension. *J. Appl. Mech.* **19**, 526–528 (1952).
22. J. P. Benthem, A Laplace transform method for the solution of semi-infinite and finite strip problems in stress analysis. *Quart. J. Mech. Appl. Math.* **16**, 413–429 (1963).
23. P. M. Morse, H. Feshbach, *Methods of Theoretical Physics* (Feshbach Publishing LLC, 1981), vol. Part I.
24. A. Košmrlj, D. R. Nelson, Statistical mechanics of thin spherical shells. *Phys. Rev. X* **7**, 011002 (2017).
25. J. Lidmar, L. Mirny, D. R. Nelson, Virus shapes and buckling transitions in spherical shells. *Phys. Rev. E* **68**, 051910 (2003).
26. D. Vella, Buffering by buckling as a route for elastic deformation. *Nat. Rev. Phys.* **1**, 425–436 (2019).
27. A. Košmrlj, D. R. Nelson, Response of thermalized ribbons to pulling and bending. *Phys. Rev. B* **93**, 125431 (2017).
28. M. Liu, L. Domino, I. Dupont de Dinechin, M. Taffetani, D. Vella, Snap-induced morphing: From a single bistable shell to the origin of shape bifurcation in interacting shells. *J. Mech. Phys. Solids* **170**, 105116 (2023).
29. J. Fierling *et al*., Embryo-scale epithelial buckling forms a propagating furrow that initiates gastrulation. *Nat. Commun.* **13**, 3348 (2022).